Chinese Journal of
POLYMER SCIENCE

RESEARCH ARTICLE

https://doi.org/10.1007/s10118-023-2973-8
Chinese J. Polym. Sci. **2023**, *41*, 1629–1637

Infrared Photodetectors and Image Arrays Made with Organic Semiconductors

Zhi-Ming Zhong†, Feng Peng†, Lei Ying*, Zhen-Qiang Huang, Wen-Kai Zhong, Gang Yu*, Yong Cao, and Fei Huang*

Institute of Polymer Optoelectronic Materials and Devices, State Key Laboratory of Luminescent Materials and Devices, South China University of Technology, Guangzhou 510640, China

Electronic Supplementary Information

Abstract Combining the strategies of introducing larger heteroatom, regio-regular backbone and extended branching position of side-chain, we developed polymer semiconductors (**PPCPD**) with narrow band-gap to construct the photosensing layer of thin-film photodiodes and image arrays. The spectral response of the resulting organic photodiodes spans from the near ultra-violet to short-wavelength infrared region. The performance of these short-wavelength infrared photodiodes in 900–1200 nm range achieved a level competitive with that of indium gallium arsenide-based inorganic crystalline detectors, exhibiting a specific detectivity of 5.55×10^{12} Jones at 1.15 μm. High photodetectivity and quantum efficiency in photodiode with amorphous/nanocrystalline thin-films of 100–200 nm thickness enabled high pixel-density image arrays without pixel-level-patterning in the sensing layer. 1 × 256 linear diode arrays with 25 μm × 25 μm pixel pitch were achieved, enabling high pixel-density short-wavelength infrared imaging at room temperature.

Keywords Conjugated polymer; Organic semiconductor; Infrared; Photodetector; Image array

Citation: Zhong, Z. M.; Peng, F.; Ying, L.; Huang, Z. Q.; Zhong, W. K.; Yu, G.; Cao, Y.; Huang, F. Infrared photodetectors and image arrays made with organic semiconductors. *Chinese J. Polym. Sci.* **2023**, *41*, 1629–1637.

INTRODUCTION

High pixel-count, low-cost, near-infrared (NIR, 700–1000 nm) and short-wavelength infrared (SWIR, 1.0–1.5 μm) focal-plane arrays have attracted broad attention due to their potential applications in artificial intelligence, such as three-dimensional face-identification, augmented/virtual reality, robotics, automatic vehicles and unmanned aerial vehicles (drones).[1–6] For example, fingerprint sensor in mobile phones has been replaced with an active-sensing infrared face-identification system, comprising a structured 940 nm laser beam, a micro-projector and a silicon-on-insulator (SOI)-based silicon photodiode array fused over a complementary metal oxide-semiconductor pixel-readout chip.[7] Despite high-intensity light-emitting diodes and laser arrays at 850 and 940 nm have been used for all-weather and security-camera systems, the long-term effects of these near-infrared light sources on the human eye remain a concern.[8] Thus, SWIR cameras (refers to the working wavelength of InGaAs photodiode) with high pixel density and large dynamic range are in high demand for various artificial intelligent systems, with those having high-power laser sources and a sensing distance range of near-eye to remote (*e.g.*, 10–100 m) being preferred.

Traditionally, SWIR photodiodes are based on crystalline germanium (Ge) and indium gallium arsenide (InGaAs). However, Ge photodiodes have a high dark current that is not suitable for weak-light sensing at room temperature. It is also difficult to pattern InGaAs and Si-based NIR photodiodes into high pixel-density sensor arrays without sacrificing their performance, as complicated dry-etching and post-etching passivation processes are required.[9–11] Infrared photodiodes can also be made from other semiconductors including low-band-gap organic semiconductors[12–14] and quantum dots.[15,16] In contrast to photodetectors based on high carrier-mobility, low defect-density single-crystal inorganic semiconductors, photodiodes based on amorphous or nanocrystalline organic semiconductors have the priority to assemble into planar, non-planar, or conformable focal plane thin-film configurations.[17–19]

The high optical absorption coefficient of organic semiconductors enables thin film photodetectors. Incident photons can be effectively absorbed in thin films of a few hundred of nanometers. Although the carrier mobility in organic semi-

* Corresponding authors, E-mail: msleiying@scut.edu.cn (L.Y.)
E-mail: gangyu@scut.edu.cn (G.Y.)
E-mail: msfhuang@scut.edu.cn (F.H.)
† These authors contributed equally to this work.
Special issue: Celebrating the 70th Anniversary of the Establishment of Polymer Program at Peking University
Received January 31, 2023; Accepted February 27, 2023; Published online April 18, 2023

conductors is lower than their inorganic counterparts, the photo-generated charge carriers formed from the absorbed photons can be effectively separated and collected at the contact electrodes with devices incorporating, for example, bulk or graded heterojunctions.[20–22] A low dark current can also be achieved, due to the low charge-defect density in the energy gap and the relatively low mobility of charge carriers. These features enable the fabrication of thin-film organic photodetectors (TFOPDs) with detectivity as good as their inorganic crystalline counterparts.[23,24] In addition, image-sensor arrays can be made with sensing pixels defined only by the bottom electrode patterns, with a non-patterned sensing layer, and the top electrode layer, such as large full-color image arrays with a large dynamic range and negligible crosstalk between neighboring pixels.[18,19,25] Large-area ultraviolet/visible image arrays for X-ray digital imagers with pixel pitches of 200 and 127 μm.[17,26,27] It is of great scientific and commercial interests to determine whether the aforementioned simple imaging array can be made from an organic semiconductor-based sensing layer that has only a patterned bottom electrode, is active in the SWIR range, and can be applied for developing small pixel-pitch, high pixel-count cameras. In this work, we introduce SWIR TFOPDs incorporating low band-gap organic semiconductor blends with performance parameters comparable to that of InGaAs. We also report the use of these SWIR TFOPDs in 1 × 256 linear sensor arrays with 25 μm pixel pitch and high-speed NIR/SWIR imaging.

EXPERIMENTAL

Synthesis of 4,4′-(4,4-Dihexadecyl-4*H*-cyclopenta[2,1-*b*:3,4-*b*′]dithiophene-2,6-diyl)bis(7-bromo-[1,2,5]selenadiazolo[3,4-*c*]pyridine)

Under the protection of nitrogen, 4,7-dibromo-[1,2,5]selenadiazolo[3,4-*c*]pyridine (0.79 g, 2.3 mmol), (4,4-dihexadecyl-4*H*-cyclopenta[2,1-b:3,4-*b*′]dithiophene-2,6-diyl)bis(trimethylstannane) (0.95 g, 1 mmol) and tetrakis (triphenylphosphine)palladium(0) ($Pd(PPh_3)_4$) (57.8 mg, 0.05 mmol) a dissolved in 30 mL of anhydrous toluene. The reaction was heated to 120 °C and stirred for 24 h. After cooling, the reaction solution was extracted with 200 mL of dichloromethane, washed with 100 mL of deionized water for three times and dried with anhydrous magnesium sulfate. After filtering and removing solvent under reduced pressure, the crude product was purified by silica column with petroleum ether:chloroform (3:1, *V*:*V*) to obtain 1.01 g of dark-blue solid, yield 88%. ^{1}H-NMR (400 MHz, $CDCl_3$, δ, ppm): 8.56 (s, 2H), 8.49 (s, 2H), 2.03 (m, 4H), 1.33–1.01 (m, 56H), 0.86 (t, J = 6.9 Hz, 6H). ^{13}C-NMR (126 MHz, $CDCl_3$, δ, ppm): 160.07, 153.32, 128.05, 110.05, 67.99, 58.50, 54.68, 37.83, 31.92, 29.96, 29.73, 29.67, 29.64, 29.58, 29.35, 26.92, 25.62, 24.70, 22.69, 18.45, 14.13. The related NMR spectra are plotted in Figs. S1 and S2 (in the electronic supplementary information, ESI).

Synthesis of PPCPD

The other monomers (4,4-dihexadecyl-4*H*-cyclopenta[2,1-*b*:3,4-*b*′]dithiophene-2,6-diyl)bis(trimethylstannane), 4,7-dibromo-[1,2,5]selenadiazolo[3,4-*c*]pyridine, 4-(2-octyldodecyl)-2,6-bis(trimethylstannyl)-4*H*-dithieno[3,2-*b*:2′,3′-*d*]pyrrole and 4-(4-octyltetradecyl)-2,6-bis(trimethylstannyl)-4*H*-dithieno[3,2-b:2′,3′-*d*]pyrrole were synthesized according to the previous reports.[28–31]

Polymer **PPCPD** was synthesized *via* Stille polymerization with the following procedure. 4,4′-(4,4-Dihexadecyl-4*H*-cyclopenta[2,1-*b*:3,4-*b*′]dithiophene-2,6-diyl)bis(7-bromo-[1,2,5]selenadiazolo[3,4-*c*]pyridine) (114.9 mg, 0.1 mmol), (4,4-dihexadecyl-4*H*-cyclopenta[2,1-*b*:3,4-*b*′]dithiophene-2,6-diyl)bis(trimethylstannane) (95.3 mg, 0.1 mmol) were dissolved in 1.5 mL of anhydrous chlorobenzene (HPLC purity). Tris(dibenzylideneacetone)dipalladium(0) (2 mg) and tris(2-methylphenyl)phosphine (4 mg) were added after the solution was carefully degassed with nitrogen for three times. Then, the reaction was sealed and heated to 140 °C for 48 h. The solution was diluted to 5 mL before cooling, then dropwise added into 200 mL of methyl alcohol. After filtering off, the precipitate was successively washed with methyl alcohol, *n*-hexane and acetone in a Soxhlet extractor, and was redissolved with chlorobenzene. After concentration, the solution was reprecipitated into 200 mL of methyl alcohol. **PPCPD** was obtained as dark-green fiber after filtration and drying in vacuum, yield 76%. The molecular weight (M_w) and polydispersity index of **PPCPD** were tested by high temperature gel permeation chromatography as 35.6 kDa and 1.68, respectively (Fig. S3 in ESI).

Fabrication of Conventional OPD and OPDIA

The copolymer **PCDTPT** and N2200 were prepared according to the procedure reported in the references.[22,29–34] $PC_{61}BM$ was purchased from Nano-C, Inc. The other reagents and chemicals were purchased from commercial sources (Aldrich, Alfa Aesar and Stream Ltd.) and used without further purification unless otherwise specified.

The OPDs were fabricated with a conventional configuration: ITO/PEDOT:PSS/active layer/LiF/Al. The indium tin oxide (ITO) coated glass substrates were cleaned by sonication in detergent, deionized water twice, acetone, and isopropyl alcohol and dried in an oven at 75 °C for 10 h. After the substrates were treated by oxygen plasma for 1 min, PEDOT:PSS (CLEVIOS™ P VP CH8000) layer as an anode buffer layer were spin-coated on ITO-coated glass substrates at 4000 r/min for 30 s, then thermally annealed at 150 °C on a hotplate for 15 min to obtain about 15 nm thin film. The blend of **PPCPD**:N2200=1:1 (*W*:*W*) or **PPCPD**:$PC_{61}BM$ = 1:1.5 (*W*:*W*) was dissolved in 2-methyl-tetrahydrofuran or chlorobenzene, respectively. By varying the rotate speed, the BHJ film thickness was kept in the range of ~130 nm, and then treated by thermal annealing at 120 °C for 10 min. Finally, the devices were finished after LiF/Al bilayer cathode (about 1 nm/90 nm) were deposited by thermal evaporation under vacuum (about 1.0×10^{-6} mbar). The device area of OPD was defined to be 0.0516 cm^2 through a shadow mask. As for OPDIA, the redundant part of function layers was removed by Q-tips dipped with solvents before cathode deposition. After shorting bar was cut, a flexible printed circuit was used to connect the OPDIA with the ROIC chip by anisotropic conductive adhesive.

Fabrication of Inverted OPD, Hole and Electron-dominant Decices

The inverted OPDs were fabricated with a configuration:

ITO/ZnO/active layer/MoO_3/Al. After the substrates were cleaned and treated by oxygen plasma for 1 min, the solution of ZnO precursor, $ZnAc_2$ were spin-coated on ITO-coated glass substrates at 4000 r/min for 30 s, then thermally annealed at 200 °C on a hotplate for 30 min in air, resulting a 30 nm-thick film. The blend of **PPCPD**:$PC_{61}BM$=1:1.5 (*W*:*W*) was dissolved in chlorobenzene, respectively. By varying the rotate speed, the BHJ film thickness was kept in the range of ~130 nm, and then treated by thermal annealing at 120 °C for 10 min. Finally, the devices were finished after MoO_3/Al bilayer cathode (about 10 nm/90 nm) were deposited by thermal evaporation under vacuum (about 1.0×10^{-6} mbar). The device area of OPD was also defined to be 0.0516 cm^2 through a shadow mask.

The configuration of hole-dominant device is ITO/PEDOT:PSS/Active layer/MoO_3/Al and the one of electron-dominant device is ITO/ZnO/Active layer/LiF/Al, with the same process above.

Characterization of OPD and OPDIA

All the measurements were carried out under ambient conditions. The thickness of the organic films was determined by a surface profiler (Bruker Dektak XT). The absorption spectra of films were measured by Shimadzu UV3600. All current density-voltage (*J*-*V*) characteristics of the devices were measured on a Keithley 236 source-meter in an electrically and optically shielded box, controlled by the computer. The intensities of the 940, 1070 and 1200 nm beams could be controlled through neutral density filters and calibrated by a low-power calibrated photodetector (Newport 818-IG/DB). The external quantum efficiency (EQE) spectrum was carried out on two commercial EQE measurement systems: QE-R (Enlitech Co., Ltd.) equipped with standard Si and Ge (RC-G108018-E) detectors and Zolix DSR100 equipped with standard Si (OSI Optoelectronics DSI200-STD-UV/UV-100L) and InGaAs (Judson DSR-A5-TE-STD/J23TE2-66C-R03M-2.6) detectors. The noise spectral density characteristics of the devices were recorded by a semiconductor parameter analyzer (Platform Design Automation, Inc. FS380 Pro^{TM}). The pulsed IR light (Thorlabs LED 940E, 1070E and 1200E) for cut-off frequency measurement was generated by LED chips and a function generator (square wave, 50% duty ratio, Tektronix AFG-1062), and we used a high-speed amplifier (FEMTO DHPCA-100) connected to a digital oscilloscope (Tektronix MDO3022) for recording data. As for 1D OPDIA, the ITO array substrates were supported by Guangzhou New Vision Optoelectronics Co., Ltd. A precision linear stages (Zolix PSA300-11-Z) and controller (Zolix MC400) were used to scan. A Texas Instruments toolkit (AFE2256EVM) and chips (AFE2256TDU) were used for read-out.

RESULTS AND DISCUSSION

Characterization of PPCPD

To achieve SWIR photodetector with response range in 1.0–1.4 μm, we developed a series of donor-acceptor type π-conjugated polymers, with relevant molecular structures and absorbance shown in Scheme 1 and Fig. S4 (in ESI).

A benchmark polymer, **PCDTPT** with regio-regular backbone was selected as chief molecular structure.[28,29] By replacing the sulphur atom in the PT unit with selenium atom, the absorption edge in **PCDTPSe** was extended to 1280 nm comparing to 1160 nm in **PCDTPT**. This can be attributable to the enhanced ground-state quinoid resonance character of selenophene.[35] The location of the nitrogen atoms in the [1,2,5]selenadiazolo[3,4-*c*]pyridine unit was precisely allocated along the vector of the backbone by tailored synthetic procedure.[28,29] To verify the advantage of regio-regular polymer, the regio-random counterpart (**rd-PCDTPSe**) was also synthesized. The optical bandgap of **rd-PCDTPSe** was 0.08 eV wider than the **PCDTPSe**, corresponding to the tendency in regio-regular and regio-random **PCDTPT**.[29]

To further extend the absorption spectra, dithieno[3,2-*b*:2',3'-*d*]pyrrole units were employed to offer stronger electron pushing effect. However, no more red-shift happened to absorption spectrum of the A-D1-A-D2 type polymer (**PPCPD-C_2**), compared to the absorption spectrum of **PCDTPSe**. It should be noted that the intramolecular charge transfer absorption peak of **PPCPD-C_2** was broad, implying lack of aggregation in film compared to the **PCDTPT** and **PCDTPSe**. To address this issue, a branch alkyl chain with extended branching position was used to eliminate the steric effects toward closer packing. Finally, a strong shoulder peak emerged at 1.1 μm, and the edge was further shifted to 1.35 μm.

Combining all the strategies and efforts, we have successfully achieved a donor polymer (denoted as **PPCPD**) with significant optic absorption in the entire NIR region and part of the SWIR region, with a strong absorption at approximately 1.1 μm and an absorption edge approaching 1.4 μm (Fig. 1a), corresponding to an optical bandgap (E_g^{opt}) of 0.92 eV. The optical absorption coefficient of polymer **PPCPD** at 0.9–1.15 μm reached 4×10^4 cm^{-1} (Fig. S4c in ESI), allowing for constructing efficient NIR and SWIR photodetectors with a sub-μm-thickness sensing layer. The lowest unoccupied molecular orbital (LUMO) and highest occupied molecular orbital (HOMO) energy levels of **PPCPD** estimated by cyclic voltammetry measurements were –3.81 and –4.74 eV, respectively. Note that these values were larger than the optical bandgap (Fig. 1b and Table S1, in ESI), as the energy derived from the solvents and the energy barrier at the two contact electrodes were involved in the former.[36,37]

Performance of Photodetectors based on PPCPD

TFOPD were prepared on conventional indium tin oxide (ITO)/glass substrates, and had a surface conductivity of 15 Ω/□ and a flat optical transmission of 85% at 500 nm. The active area of each testing TFOPD device was 0.0516 cm^2, as defined by the overlap areas between the bottom ITO and the top cathode. The device structure is ITO/PEDOT:PSS (15 nm)/active layer/LiF/Al, and the active layer was composed of **PPCPD** and an n-type molecule $PC_{61}BM$ or the polymer N2200 (Fig. S4a in ESI). As shown in Figs. 1(c) and 1(d), although the built-in field was relatively small, as indicated by the open circuit voltage (V_{OC}) of about 0.2 V (*i.e.*, the voltage corresponding to the minimum in $|J_{ph}|$ that is close to the flat-band condition in the diode), the photocurrent (J_{ph}) increased drastically with reversed bias. When the bias was sufficiently large, the J_{ph} enters a $V<V_1$ regime (where the V_1 is defined as the voltage at the tangency point of the photocurrent curve and the extension of its linear part), in which the magnitude of J_{ph} increased with the reverse bias following the relation $J_{ph} = J_{ph}(0)\exp(-V/V_0)$, with V_0~3 V for both devices.

https://doi.org/10.1007/s10118-023-2973-8

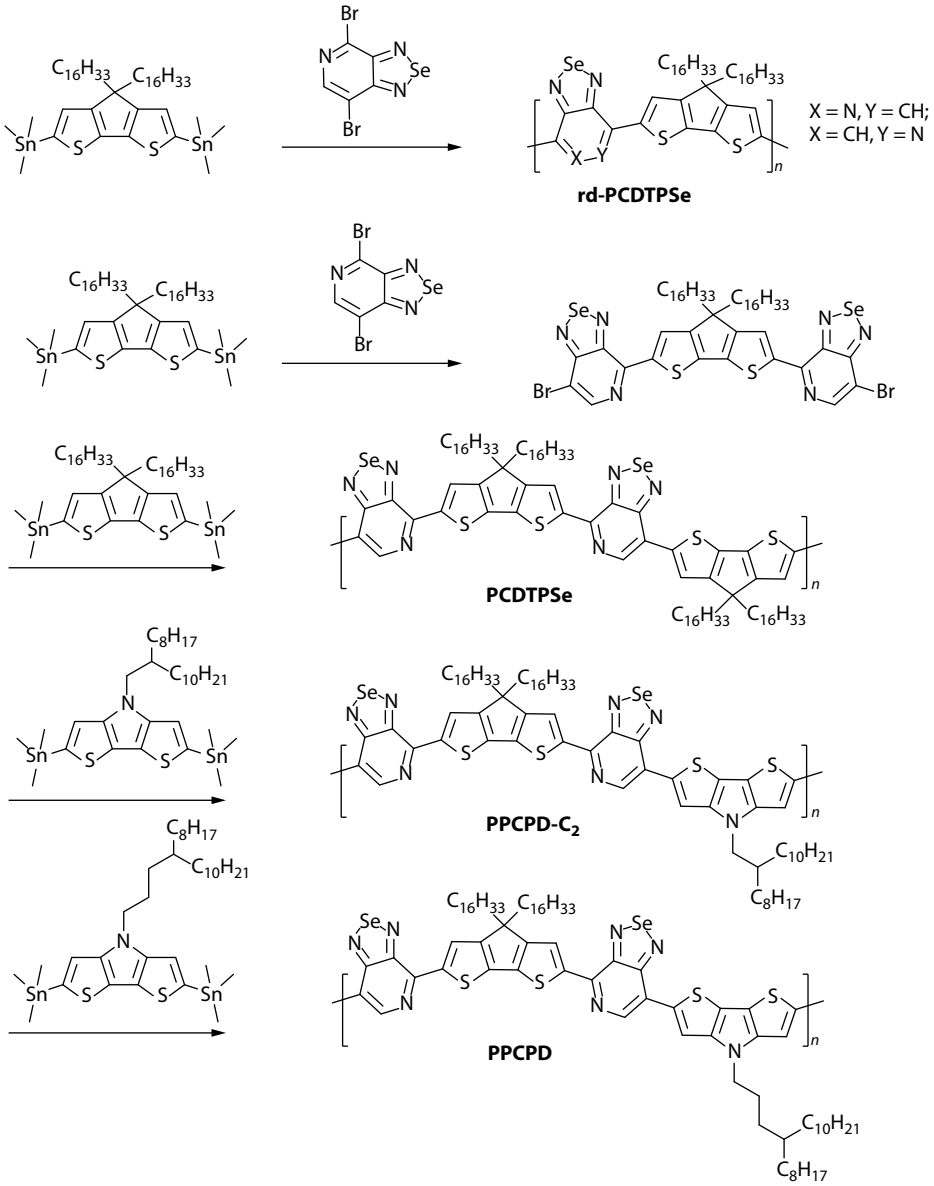

Scheme 1 Synthesis of narrow bandgap of polymers.

The device that incorporated **PPCPD**:$PC_{61}BM$ had a V_1 of about –50 mV and a $|V_1 - V_{built\text{-}in}|$ of 0.3 V (wherein the $V_{built\text{-}in}$ was estimated to be approximately V_{OC} of about 0.3 V, measured under 100 mW·cm^{-2} solar simulator). The **PPCPD**:N2200 device had a V_1 of –0.2 V, a V_{OC} of 0.35 V and $|V_1 - V_{built\text{-}in}|$ of 0.55 V. When Reverse bias $V<V_1$, the photoinduced carrier can be effectively collected by contact electrodes. In the narrow gap (<1 eV) **PPCPD**, one just needs <4×10^4 V·cm^{-1} to separate and collect the charges, which is a relative low field. These results reveal that when E_g^{opt} of polymer donor is reduced to 1 eV and E_{LUMO} (donor) – E_{LUMO} (acceptor) = ΔE_{LUMO} equates to 0.44 eV (for **PPCPD**:N2200) and 0.60 eV (for **PPCPD**:$PC_{61}BM$), the photoinduced charge carriers can still be effectively separated and collected at the contact electrodes once the effective biasing is >0.5 V. At V=–0.1 V, the J_d is 2.16 nA·cm^{-2} for **PPCPD**:$PC_{61}BM$ and 3.51 nA·cm^{-2} for **PPCPD**:N2200, which are substantially lower than those of crystalline InGaAs photodiodes used in the SWIR range (~ 100–250 nA·cm^{-2}, Table 1).

Fig. 2 and Fig. S5 (in ESI) show the photoresponsivity (R), external quantum efficiency (EQE) and specific detectivity D^* of TFOPDs. It can be seen that at V=–0.1 V, the peak photoresponsivity of the **PPCPD**:$PC_{61}BM$ device reaches 0.14 A·W^{-1}, and the corresponding peak EQE of ~17%, and the specific detectivity D^* (–0.1 V) of 5.55×10^{12} Jones (at 1.15 μm). In the D^* calculation, the noise power was assumed to be dominated by dark-current noise, which was valid for high-frame-rate imaging applications. Consistent with the *J-V* curve (Figs. 1c and 1d), the photocurrent dramatically increased with the reverse bias varied from 0 V to –1 V, while the peak photoresponsivity (R) and EQE reached 0.23 A·W^{-1} and 27% at –1 V, respectively. A similar voltage-dependence was also observed in a TFOPD made with **PPCPD**:N2200, wherein at –1 V bias, the infrared peak photoresponsivity and EQE were 0.12 A·W^{-1} and 14%, respectively. The hole mobility in the

https://doi.org/10.1007/s10118-023-2973-8

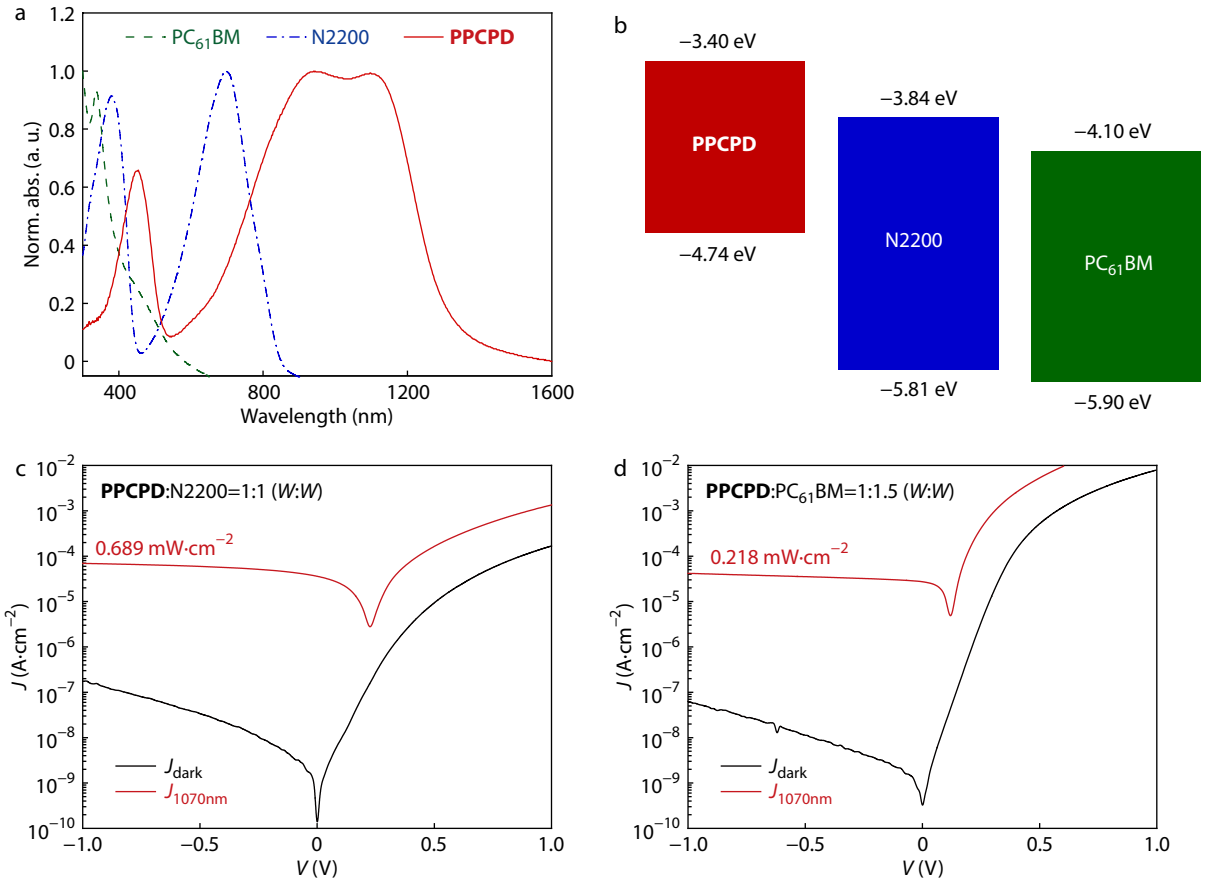

Fig. 1 (a) Normalized absorption spectra of corresponding films; (b) Energy level alignments; (c) J_d and J_{ph} of ITO/PEDOT:PSS/**PPCPD**:N2200=1:1 (*W*:*W*)/LiF/Al and (d) ITO/PEDOT:PSS/**PPCPD**:$PC_{61}BM$=1:1.5 (*W*:*W*)/LiF/Al. The data in black were obtained in the dark, the data in red were obtained under 1.07 μm light illumination, supplied through the glass/ITO side and generated by a 1.07 μm-light emitting diode.

Table 1 Performance comparison of SWIR detectors.

Device	Wavelength (nm)	*R* at 1.15 μm (A·W^{-1})	EQE at 1.15 μm	D^* (cm·Hz$^{1/2}$·W^{-1})
PPCPD:$PC_{61}BM$ TFOPD	300–1300	0.136 (–0.1 V) 0.517 (–0.9V, inverted)	14.76% (–0.1 V) 56.2% (–0.9 V, inverted)	5.55×10^{12} (–0.1 V, 1.15 μm) 8.95×10^{10} (–0.9 V, 1.15 μm)
PPCPD:2200 TFOPD	300–1300	0.077 (–0.1 V)	8.40 % (–0.1 V)	3.08×10^{12} (–0.1 V, 1.15 μm)
InGaAs [a] PIN	900–1700	0.75 (–0.1 or –0.9 V)	80% (–0.1 or –0.9 V)	3.7×10^{12} (1.15 μm) 5.0×10^{12} (1.55 μm)

[a] InGaAs Photodiodes_Selection Guide: April 2021, Hamamatsu K.K., www.hamamatsu.com, (Hamamatsu G8370-10).

PPCPD:$PC_{61}BM$ and **PPCPD**:N2200 blends was in the order of 10^{-5} cm^2·V^{-1}·s^{-1} (Fig. S6 in ESI). These mobility data are consistent with the higher photoresponsivity and EQE in the **PPCPD**:$PC_{61}BM$-based device. In addition, a comparison of the optical absorption shown in Fig. 1(a) with the data shown in Fig. 2 reveals that the photoresponsivity and EQE in **PPCPD**:$PC_{61}BM$ over the entire visible and infrared spectral ranges are primarily influenced by the photoexcited electrons and holes in **PPCPD**, while the photoresponsivity and EQE in **PPCPD**:N2200 are enhanced in the range of 500–800 nm due to the strong optical absorption in N2200 over the same range. Although there is stronger optical absorption in **PPCPD**:N2200 at 700 nm, the *R* and EQE in **PPCPD**:N2200 remain the same as in **PPCPD**:$PC_{61}BM$ due to the smaller LUMO energy difference between **PPCPD** and N2200 and the lower electron mobility in N2200. These properties also result in **PPCPD**:N2200 exhibiting approximately half the magnitude of *R* and EQE in the SWIR comparing to that exhibited by **PPCPD**:$PC_{61}BM$ (Fig. 2).

Fig. 2 and Fig. S5 (in ESI) also show the photoresponsivity and EQE of a **PPCPD**:$PC_{61}BM$ OPD in reversed configuration, in which light illumination is still provided from the glass/ITO side into the TFOPD. The device was constructed with structure of ITO/ZnO (30 nm)/sensing layer/MoO_3 (15 nm)/Al (90 nm), and the thickness of the **PPCPD**:$PC_{61}BM$ sensing layer was approximately 130 nm. This configuration device demonstrated a similar voltage dependence to that exhibited by the conventional device (see Figs. 2a and 2b). The peak photo-

https://doi.org/10.1007/s10118-023-2973-8

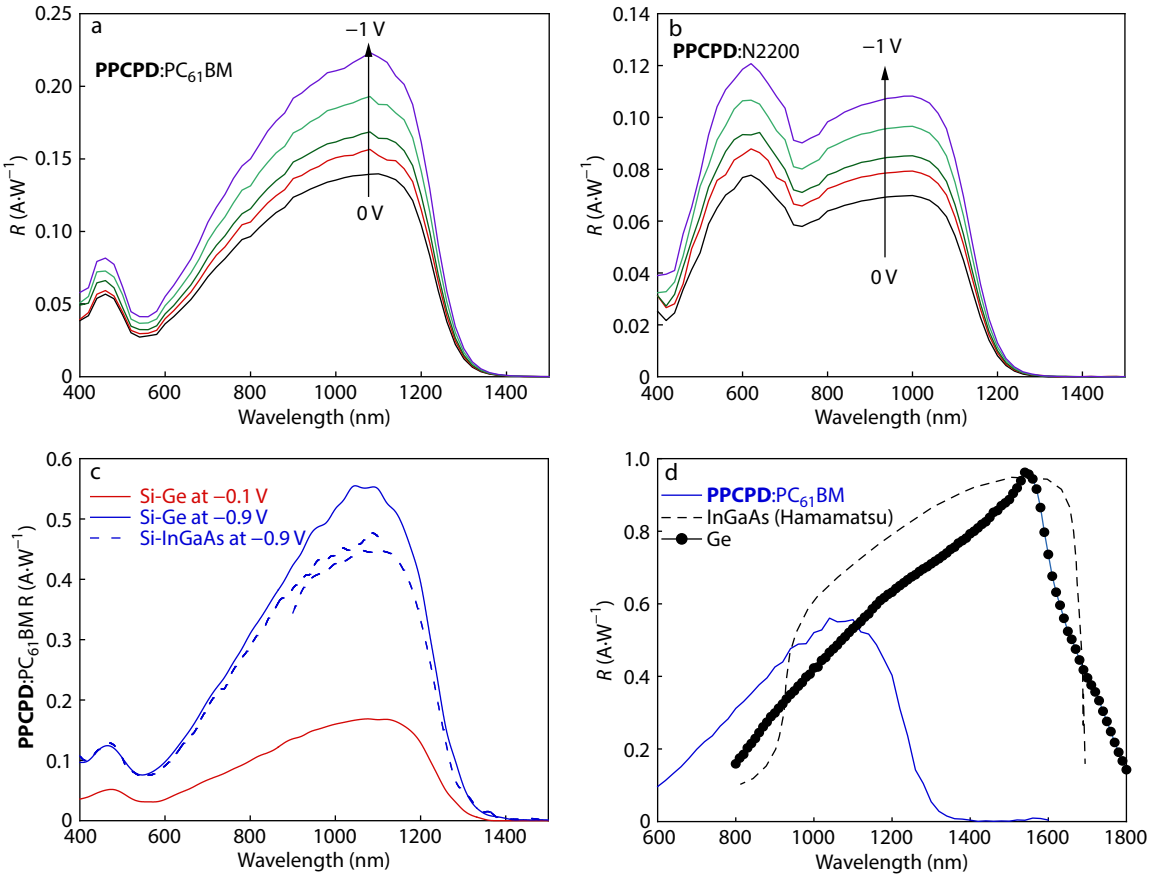

Fig. 2 (a) Energy level alignments, (b) normalized absorption spectra of corresponding films. (c) J_d and J_{ph} of ITO/PEDOT:PSS/**PPCPD**:N2200=1:1 (*W*:*W*)/LiF/Al and (d) ITO/PEDOT:PSS/**PPCPD**:$PC_{61}BM$=1:1.5 (*W*:*W*)/LiF/Al. The data in black were obtained in the dark, the data in red were obtained under 1.07 μm light illumination, supplied through the glass/ITO side and generated by a 1.07 μm-light emitting diode.

responsivity (Fig. 2c) and EQE (Fig. S5h in ESI) are 0.17 A·W^{-1} and 20% at –0.1 V bias, respectively. At –0.9 V bias, and these increased to 0.46 A·W^{-1} (calibrated with an InGaAs reference photodiode, Judson DSR-A5-TE-STD/J23TE2-66C-R03M-2.6) and 0.56 A·W^{-1} (calibrated with a Ge reference photodiode, RC-G108018-E) for *R*. The corresponding EQE at *V*=–0.9 V are 55% and 65%. In Fig. 2(d), the *R* of the **PPCPD**:$PC_{61}BM$ at –0.9 V bias could be compared with that from the reference InGaAs and Ge photodiodes, and it can be seen that both *R* and EQE are similar in value to those of their inorganic counterparts containing InGaAs and Ge. For example, at 1.1 μm, R_{TFOPD}=0.55 A·W^{-1} and R_{InGaAs}=0.7 A·W^{-1}; while at 1.2 μm, R_{TFOPD}=0.4 A·W^{-1} and R_{InGaAs}=0.8 A·W^{-1}.

In Table 1, we compare the performance parameters of SWIR TFOPDs with those from two high-specification InGaAs photodiodes manufactured by Hamamatsu K. K. The special detectivity of these polymeric SWIR TFOPDs reaches or surpasses the value exhibited by the InGaAs photodiodes (3.7×10^{12} Jones). Thus, our polymeric SWIR photodiodes are efficacious and economic components for incorporation into commercial devices operating in the NIR/SWIR wavelength range. The data in Figs. S7(a) and S7(b) (in ESI) also show that the photocurrent has a linear response over four orders of magnitude greater than the input light intensity, and fast response times (*e.g.*, ~10^{-4} s in a device of 0.0516 mm^2, as seen in Figs. S7c–S7f in ESI) were also observed. Both features render these polymeric TFOPDs ideally suited for use in pixel-element devices for SWIR image arrays.

Linear Array for Infrare Image Sensing

In the early round of organic photodiode development, it was demonstrated that visible-light TFOPDs can be used in large-size image array applications that have a simple array architecture: *i.e.*, where pixel definition is achieved with only a patterned bottom electrode and an unpatterned sensing layer.[26] In this work, we explored if such array structure (Fig. 3) could be used in infrared cameras, referring to the design of high pixel-density InGaAs imager.[38] Fig. 3(b) shows a photograph of two 1 × 256 linear image arrays (TFOPDIA, 25 μm × 25 μm pixel pitch, 68% aperture ratio, 6.25 mm sensing length) in which the top array is connected to a readout-integrating circuit (ROIC) chip (Texas Instrument, AFE2256) mounted on a flex connector. A two-dimensional SWIR imaging system is achieved by mounting the linear TFOPDIA onto a translation stage to enable vertical scanning with a 25 μm shifting step (Fig. 3a). Two SWIR images captured with this imaging scanner are shown in Figs. 3(e) and 3(g). For comparison, the corresponding visible colored images taken with a smartphone camera (from back camera of iPhone 6s plus, 1200M pixels, aside the beam path) are shown in Figs. 3(d) and

https://doi.org/10.1007/s10118-023-2973-8

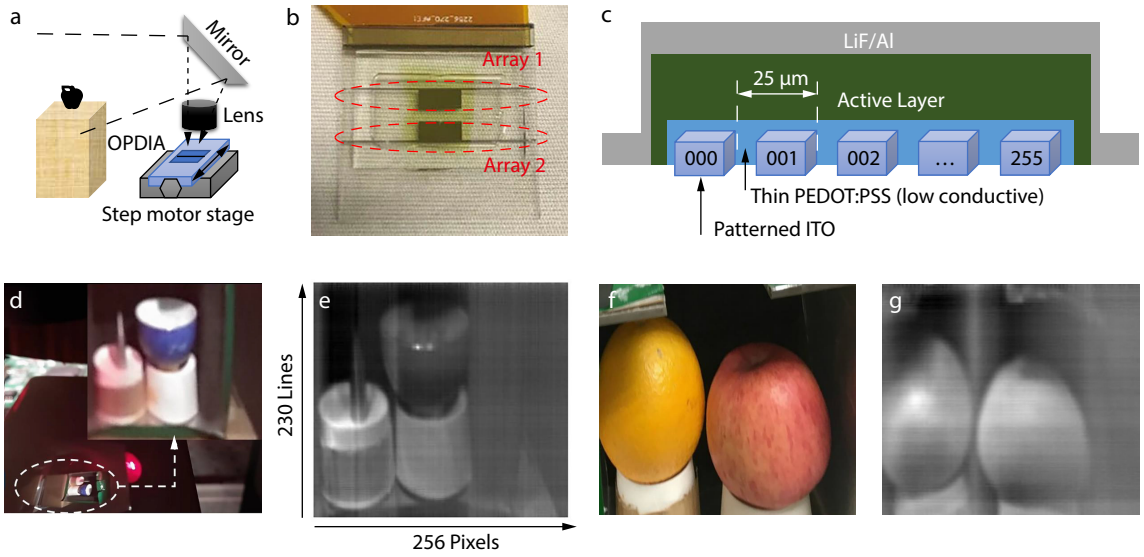

Fig. 3 (a) The SWIR imaging system, (b) top view of the OPDIA arrays arranged on a 30 mm × 30 mm glass substrate, and (c) the cross-section sketch of the OPDIA; (d) The perspective view of how input image (insert) cast on the OPDIA and (e) the result image scanned *via* OPDIA. Because the focal plane is adjusted to the OPDIA beneath the glass substrate, thus the image displayed on the surface of glass substrate is a little blur; (f) The photos of the original input objects and (g) the resulted image.

3(f). The SWIR light source comprised an IR lamp and an IR pass optical filter. The resulting SWIR images comprised 256 × 230 imaging elements, and a sampling time of 100 μs was used, which is equivalent to image-capturing at 10 kHz. This performance of our organic photodiode-based array-based image array was equivalent to the maximum frame rate of a 25 μm pitch, 1 × 256 linear image array made from high-specification InGaAs wafers.[38] The detailed *I-V* characteristics of adjacent ITOs was measured and discussed in Fig. S12 in ESI.

It is well-known that the crystalline quality of semiconductors is vitally important to the performance of photodiodes, with purity and defect density in the depleted layer strongly influencing photoinduced carriers, the dark current and noise levels. This is due to the high carrier mobility of photodiodes, which renders them sensitive to defect density in the crystalline semiconductor sensing layer. As such, deep-trench isolation (DTI) is required between neighboring pixels in sensing arrays to eliminate electrical crosstalk between neighbor pixels. For example, a Si-based CMOS imager for NIR applications at 880 and 940 nm requires a thick intrinsic layer, as used in the reverse-illuminated CMOS imager or an SOI image sensor layer with a sensing layer patterned at the pixel level *via* the DTI process.[10,11] A similar process is required for the construction of image arrays that function in the SWIR range, such as the sensing array made with InGaAs.[9]

The SOI and InGaAs sensing arrays need to be bonded with a two-dimensional (2D) CMOS circuit readout array patterned in the same form factor.[8–10] The DTI insulation process involves dry-etching and post-etching passivation to eliminate the defects generated near the exposed surfaces. The required quality of the post-etching surface repair increases as the demands for pixel-pitch reduction and the trench-depth elongation (*i.e.*, the ratio of the increase in surface area to the sensing volume) increase. In this context, the use of amorphous/nanocrystalline TFOPDIA enables another approach for fabrication of high pixel-density NIR/SWIR image arrays. As shown in the results of grazing-incidence wide-angle X-ray scattering (GIWAXS, Fig. S8 in ESI) and atomic force microscopy image (AFM, Fig S9 in ESI), there were lack of long-range order in both the **PPCPD**:N2200 and **PPCPD**:$PC_{61}BM$ thin films. Thus, combining the moderate carrier mobility (10^{-5} $cm^2 \cdot V^{-1} \cdot s^{-1}$, Fig. S6 in ESI) with high absorption coefficient at sensing wavelengths (and thus at the 130 nm-thick sensing layer), the array structure shown in Fig. 3(c) can be adopted, without patterning of the sensing layer or the other, upper layers being required.

In this design, the sensor pixilation is fully defined by the bottom electrode pad, which can be assembled using processes typically employed in existing MOSFET or TFT manufacturing facilities. Thus, these data show that high information-content imaging can be achieved with an OPDIA of 25 μm pixel pitch. This represents the first validation of the applicability of OPDIA without pixel-level patterning in the sensing layer in high information-content SWIR imagers and cameras. The simple structure of OPDIAs and their amenability to add-on process flow-based incorporation into TFOPDIA products will enable a sound business model to developed, resulting in rapid market adoption.

The peak photoresponsivity in Fig. 2 is at ~1.15 μm; this is, in fact, the desired operational wavelength for 3D-active-sensing in outdoor environments, as it is the next solar radiation minima after 940 nm. 3D-active-imaging operating at ~1.15 μm is subject to substantially less sunlight disturbance than that at 940 nm, and thus better detectivity can be achieved. The sensitivity of the human eye at 1.15 μm is also substantially lower than that at 940 nm,[39] and thus higher excitation power densities or exposure time can be safely used at ~1.15 μm to increase the detectivity and the detecting distance of the active-sensing system.[8] This will be invaluable for improved artificial intelligence, robotics, and automatic car applications.

Technically, the dark current could be suppressed by fur-

ther reducing the traps densities (Fig. S10 in ESI) and introducing charge blocking layers with suitable energy levels and charge mobilities. Using such a semi-conducting interlayer to replace the conductive PEDOT:PSS might also reduce the cross-talk current (Fig. S11 in ESI) and improve image quality. Cooling system could also be an option to improve the performance (Fig. S12 in ESI).

CONCLUSIONS

In summary, organic semiconductors with narrow energy gaps of 0.92 eV were achieved by use of novel polymeric materials capable of intramolecular charge transfer between electron donor group and acceptor groups. The organic semiconductors were used as photosensing layers in thin-film photodiode arrays, and the spectral response of the fabricated OPDIAs spanned the near UV (<400 nm), visible (400–700 nm), near-infrared (700–1000 nm) and short-wavelength infrared (SWIR, 1.0–1.4 μm), a wider spectral range than their inorganic counterparts. The performance of these SWIR photodiodes at 900–1200 nm was optimized to a level competitive with that of InGaAs-based inorganic crystalline detectors, exhibiting a specific detectivity of 5×10^{12} Jones at 1.15 μm. High SWIR photodetectivity and quantum efficiency were achieved in amorphous/nanocrystalline thin-films of 100–200 nm thickness, enabling high pixel-density image arrays to be made without pixel-level-patterning being required in the sensing layer. OPDIAs containing 1 × 256 linear diode arrays with 25 μm × 25 μm pixel pitch were fabricated, and the 1 × 256 array was demonstrated to be capable of high pixel-density SWIR imaging at room temperature.

Conflict of Interests

The authors declare no interest conflict.

Electronic Supplementary Information

Electronic supplementary information (ESI) is available free of charge in the online version of this article at http://doi.org/10.1007/s10118-023-2973-8.

ACKNOWLEDGMENTS

This work was financially supported by the National Natural Science Foundation of China (Nos. U21A6002 and 51933003) and the Basic and Applied Basic Research Major Program of Guangdong Province (No. 2019B030302007).

REFERENCES

1 Manna, E.; Xiao, T.; Shinar, J.; Shinar, R. Organic photodetectors in analytical applications. *Electronics* **2015**, *4*, 688–722.
2 Zhu, D.; Ji, D.; Li, L.; Hu, W. Recent progress in polymer-based infrared photodetectors. *J. Mater. Chem. C* **2022**, *10*, 13312–13323.
3 Cao, Y.; Yang, X.; Liu, C.; Huang, F. Application of organic/polymer photodetectors in the medical and healthcare area. *Acta Polymerica Sinica* (in Chinese) **2022**, *53*, 307–330.
4 Ren, H.; Chen, J.; Li, Y.; Tang, J. Recent progress in organic photodetectors and their applications. *Adv. Sci.* **2021**, *8*, 2002418.
5 Yang, W.; Qiu, W.; Georgitzikis, E.; Simoen, E.; Serron, J.; Lee, J.; Lieberman, I.; Cheyns, D.; Malinowski, P.; Genoe, J.; Chen, H.; Heremans, P. Mitigating dark current for high-performance near-infrared organic photodiodes *via* charge blocking and defect passivation. *ACS Appl. Mater. Interfaces* **2021**, *13*, 16766–16774.
6 Pan, Y.; Tao, L.; Gao, J.; He, C.; Liu, Z.; Fang, Y.; Shi, M.; Chen, H. A near-infrared electron acceptor with thieno[3,4-*b*]thiophene as the core and the related high-performance photodetectors. *Acta Polymerica Sinica* (in Chinese) **2022**, *53*, 424–432.
7 Rob Verger, "Apple's new face ID system uses a sensing strategy that dates back decades", Popular Science, Sept. 13, **2017**, https://www.popsci.com/apple-face-ID/.
8 International Electrotechnical Commission, "IEC 60825-1–Safety of laser products – Part 1: Equipment classification and requirements", 3.0 edition (**2014**)).
9 Fan, D.; Lee, K.; Forrest, S. R. Flexible thin-film InGaAs photodiode focal plane array. *ACS Photonics* **2016**, *3*, 670–676.
10 Hashimoto, T.; Satoh, H.; Fujiwara, H.; Arai, M. A study on suppressing crosstalk through a thick SOI substrate and deep trench isolation. *IEEE J. Electron Devices Soc.* **2013**, *1*, 155–161.
11 Lee, S.; Bashir, R. Modeling and characterization of deep trench isolation structures. *Microelectron. J.* **2001**, *32*, 295–300.
12 Gong, X.; Tong, M.; Xia, Y.; Cai, W.; Moon, J. S.; Cao, Y.; Yu, G.; Shieh, C. L.; Nilsson, B.; Heeger, A. J. High-detectivity polymer photodetectors with spectral response from 300 nm to 1450 nm. *Science* **2009**, *325*, 1665–1667.
13 Wu, Z.; Zhai, Y.; Kim, H.; Azoulay, J. D.; Ng, T. N. Emerging design and characterization guidelines for polymer-based infrared photodetectors. *Acc. Chem. Res.* **2018**, *51*, 3144–3153.
14 Li, Q.; Guo, Y.; Liu, Y. Exploration of near-infrared organic photodetectors. *Chem. Mater.* **2019**, *31*, 6359–6379.
15 Saran, R.; Curry, R. J. Lead sulphide nanocrystal photodetector technologies. *Nat. Photon.* **2016**, *10*, 81–92.
16 Hafiz, S.; Scimeca, M.; Sahu, A.; Ko, D. Colloidal quantum dots for thermal infrared sensing and imaging. *Nano Convergence* **2019**, *6*, 1–22.
17 Gelinck, G. H.; Kumar, A.; van der Steen, J. L.; Shafique, U.; Malinowski, P. E.; Myny, K.; Rand, B. P.; Simon, M.; Rütten, W.; Douglas, A. X-ray imager using solution processed organic transistor arrays and bulk heterojunction photodiodes on thin, flexible plastic substrate. *Org. Electron.* **2013**, *14*, 2602–2609.
18 Tordera, D.; Peeters, B.; Akkerman, H. B.; van Breemen, A. J.; Maas, J.; Shanmugam, S.; Kronemeijer, A. J.; Gelinck, G. H. A high-resolution thin-film fingerprint sensor using a printed organic photodetector. *Adv. Mater. Technol.* **2019**, *4*, 1900651.
19 Ng, T. N.; Wong, W. S.; Chabinyc, M. L.; Sambandan, S.; Street, R. A. Flexible image sensor array with bulk heterojunction organic photodiode. *Appl. Phys. Lett.* **2008**, *92*, 213303.
20 Yu, G.; Gao, J.; Hummelen, J. C.; Wudl, F.; Heeger, A. J. Polymer photovoltaic cells: enhanced efficiencies *via* a network of internal donor-acceptor heterojunctions. *Science* **1995**, *270*, 1789–1791.
21 Yu, G.; Heeger, A. J. Charge separation and photovoltaic conversion with internal donor/acceptor heterojunctions in polymer composites. *J. Appl. Phys.* **1995**, *78*, 4510–4515.
22 Zhong, Z.; Bu, L.; Zhu, P.; Xiao, T.; Fan, B.; Ying, L.; Lu, G.; Yu, G.; Huang, F.; Cao, Y. Dark current reduction strategy *via* a layer-by-layer solution process for a high-performance all-polymer photodetector. *ACS Appl. Mater. Interfaces* **2019**, *11*, 8350–8356.
23 Yang, D.; Ma, D. Development of organic semiconductor photodetectors: from mechanism to applications. *Adv. Opt. Mater.* **2019**, *7*, 1800522.
24 Yu, G.; Srdanov, G.; Wang, H.; Cao, Y.; Heeger, A. J. Photovoltaic

cells and photodetectors made with semiconductor polymers: recent progress. *Org. Photon. Mater. Devices II* **2000**, *3939*, 118–125.
25 Gasparini, N.; Gregori, A.; Salvador, M.; Biele, M.; Wadsworth, A.; Tedde, S.; Baran, D.; McCulloch, I.; Brabec, C. Visible and near-infrared imaging with nonfullerene-based photodetectors. *Adv. Mater. Technol.* **2018**, *3*, 1800104.
26 Yu, G.; Wang, J.; McElvain, J.; Heeger, A. J. Large-area, full-color image sensors made with semiconducting polymers. *Adv. Mater.* **1998**, *10*, 1431–1434.
27 Yu, G.; Shieh, C. L.; Xiao, T.; Lee, K.; Foong, F.; Wang, G.; Musolf, J.; Chen, Z.; Chang, F.; Ottosson, K. High throughput motft with organic etch-stopper and sinx gate insulator. *SID Symp. Dig. Technol. Pap.* **2015**, *46*, 296–299.
28 Ying, L.; Huang, F.; Bazan, G. C. Regioregular narrow-bandgap-conjugated polymers for plastic electronics. *Nat. Commun.* **2017**, *8*, 1–13.
29 Ying, L.; Hsu, B. B.; Zhan, H.; Welch, G. C.; Zalar, P.; Perez, L. A.; Kramer, E. J.; Nguyen, T. Q.; Heeger, A. J.; Wong, W. Y. Regioregular pyridal [2,1,3] thiadiazole π-conjugated copolymers. *J. Am. Chem. Soc.* **2011**, *133*, 18538–18541.
30 Ming, S.; Zhen, S.; Liu, X.; Lin, K.; Liu, H.; Zhao, Y.; Lu, B.; Xu, J. Chalcogenodiazolo [3,4-*c*] pyridine based donor-acceptor-donor polymers for green and near-infrared electrochromics. *Polym. Chem.* **2015**, *6*, 8248–8258.
31 Brebels, J.; Klider, K. C.; Kelchtermans, M.; Verstappen, P.; Van Landeghem, M.; Van Doorslaer, S.; Goovaerts, E.; Garcia, J. R.; Manca, J.; Lutsen, L. Low bandgap polymers based on bay-annulated indigo for organic photovoltaics: enhanced sustainability in material design and solar cell fabrication. *Org. Electron.* **2017**, *50*, 264–272.
32 Li, M. J.; Fan, B. B.; Zhong, W. K.; Zeng, Z. M. Y.; Xu, J. K.; Ying, L. Rational design of conjugated polymers for d-limonene processed all-polymer solar cells with small energy loss. *Chinese J. Polym. Sci.* **2020**, *38*, 791–796.
33 Wang, X.; Gao, S. J.; Han, J. F.; Zhang, Y. L.; Zhang, S.; Qiao, W. Q.; Wang, Z. Y. Effect of 1, 8-diiodooctane content on the performance of P3HT: $PC_{61}BM$ bulk heterojunction photodetectors. *Chinese J. Polym. Sci.* **2021**, *39*, 831–837.
34 Xie, B.; Zhang, K.; Li, J.; Li, L.; Song, Y.; Cui, N.; Bai, Y.; Huang, F. High-sensitivity visible-blind near-infrared narrowband organic photodetectors realized by controlling trap distribution. *Acta Polymerica Sinica* (in Chinese) **2022**, *53*, 414–423.
35 Gibson, G. L.; Seferos, D. S. P. "Heavy-atom" donor-acceptor conjugated polymers. *Macromol. Chem* **2014**, *215*, 811–823.
36 Sworakowski, J.; Janus, K. On the reliability of determination of energies of HOMO levels in organic semiconducting polymers from electrochemical measurements. *Org. Electron.* **2017**, *48*, 46–52.
37 Pho, T. V.; Toma, F. M.; Tremolet de Villers, B. J.; Wang, S.; Treat, N. D.; Eisenmenger, N. D.; Su, G. M.; Coffin, R. C.; Douglas, J. D.; Fréchet, J. M. Decacyclene triimides: paving the road to universal non-fullerene acceptors for organic photovoltaics. *Adv. Energy Mater.* **2014**, *4*, 1301007.
38 Hamamatsu, G9203-256D, line rate of 1KHz, Selection Guide of InGaAs Photodiodes, p. 6,11&13, April **2021**; https://www.hamamatsu.com/resources/pdf/ssd/infrared_kird0001e.pdf.
39 Griffin, D. R.; Hubbard, R.; Wald, G. The sensitivity of the human eye to infra-red radiation. *J. Opt. Soc. Am. A* **1947**, *37*, 546–554.

https://doi.org/10.1007/s10118-023-2973-8